https://doi.org/10.1038/s41586-018-0807-6

Observation of the nonlinear Hall effect under time-reversal-symmetric conditions

Qiong Ma[1,13], Su-Yang Xu[1,13], Huitao Shen[1,13], David MacNeill[1], Valla Fatemi[1], Tay-Rong Chang[2], Andrés M. Mier Valdivia[1], Sanfeng Wu[1], Zongzheng Du[3,4,5], Chuang-Han Hsu[6,7], Shiang Fang[8], Quinn D. Gibson[9], Kenji Watanabe[10], Takashi Taniguchi[10], Robert J. Cava[9], Efthimios Kaxiras[8,11], Hai-Zhou Lu[3,4], Hsin Lin[12], Liang Fu[1], Nuh Gedik[1]* & Pablo Jarillo-Herrero[1]*

The electrical Hall effect is the production, upon the application of an electric field, of a transverse voltage under an out-of-plane magnetic field. Studies of the Hall effect have led to important breakthroughs, including the discoveries of Berry curvature and topological Chern invariants[1,2]. The internal magnetization of magnets means that the electrical Hall effect can occur in the absence of an external magnetic field[2]; this 'anomalous' Hall effect is important for the study of quantum magnets[2–7]. The electrical Hall effect has rarely been studied in non-magnetic materials without external magnetic fields, owing to the constraint of time-reversal symmetry. However, only in the linear response regime—when the Hall voltage is linearly proportional to the external electric field—does the Hall effect identically vanish as a result of time-reversal symmetry; the Hall effect in the nonlinear response regime is not subject to such symmetry constraints[8–10]. Here we report observations of the nonlinear Hall effect[10] in electrical transport in bilayers of the non-magnetic quantum material WTe_2 under time-reversal-symmetric conditions. We show that an electric current in bilayer WTe_2 leads to a nonlinear Hall voltage in the absence of a magnetic field. The properties of this nonlinear Hall effect are distinct from those of the anomalous Hall effect in metals: the nonlinear Hall effect results in a quadratic, rather than linear, current–voltage characteristic and, in contrast to the anomalous Hall effect, the nonlinear Hall effect results in a much larger transverse than longitudinal voltage response, leading to a nonlinear Hall angle (the angle between the total voltage response and the applied electric field) of nearly 90 degrees. We further show that the nonlinear Hall effect provides a direct measure of the dipole moment[10] of the Berry curvature, which arises from layer-polarized Dirac fermions in bilayer WTe_2. Our results demonstrate a new type of Hall effect and provide a way of detecting Berry curvature in non-magnetic quantum materials.

In 1879 Edwin H. Hall observed that when an electric current passed through a gold film under a magnetic field, a transverse voltage developed. This effect, known as the Hall effect, forms the basis of fundamental research and practical applications, such as magnetic field measurements and motion detectors. In contrast to the classical Hall effect, whereby the Lorentz force bends the trajectories of charge carriers, quantum mechanics describes the 'bending' via the intrinsic geometry of the quantum electron wavefunctions under time-reversal-symmetry breaking. This theoretical understanding led to the discoveries of Berry curvature and topological Chern numbers, both of which have become essential in modern condensed matter physics[1,2]. An important area of research involves identifying a quantized or topological anomalous Hall effect in unconventional magnetic quantum materials, in which spin–orbit coupling, geometric frustration and electronic correlations coexist[2–7]. These previous studies[2–7] established a paradigm for the electrical Hall effect: (1) a non-vanishing Hall conductivity that arises from the momentum-integrated Berry curvature; (2) a Hall voltage that is linearly proportional to the external electric field; and (3) a Hall conductivity that (except in the quantum Hall regime) is a fraction of the longitudinal conductivity, as measured by the Hall angle. The first property requires breaking of time-reversal symmetry and is realized, for example, in magnets or by applying magnetic fields (Fig. 1a, b). However, electrical Hall effects beyond this paradigm are theoretically possible.

Whereas Hall effects in the linear response regime (linear Hall effects) must exhibit the properties described above, those in the nonlinear response regime (nonlinear Hall effects) are not subject to the same constraints and so may have distinct characteristics. Building on previous theoretical work[8,9], a second-order nonlinear Hall effect was proposed recently[10]. This theoretical study[10] points out that, in addition to the momentum-integrated Berry curvature that is responsible for the linear Hall effect, there are other important properties concerning the Berry curvature. In particular, even in a non-magnetic material, inversion-symmetry breaking may segregate the positive and negative Berry curvatures in different momentum (k) regions (Fig. 1d), leading to a dipole moment. Such a Berry-curvature dipole should give rise to an electrical Hall effect[10], albeit in the second-order response; as depicted in Fig. 1c, a nonlinear Hall effect is induced by an electric field parallel to the Berry-curvature dipole $\boldsymbol{\Lambda}$. The various experimental consequences of Berry-curvature dipoles are still being explored[10–12], but the possibility of realizing electrical Hall effects in non-magnetic materials has already attracted great interest[13–20]. We considered candidate materials according to the following three criteria: the existence of Berry-curvature hotspots, of the desired crystalline symmetry properties and of additional experimental tuning parameters. We identified bilayers of the quantum material WTe_2 as an ideal material (see Supplementary Information section I).

WTe_2 has attracted much interest recently because of its remarkable properties both in the bulk and in monolayers[21–29]. In particular, monolayer WTe_2 has a high-temperature quantum spin Hall state[23,25–27] and gate-tunable superconductivity[28,29]. On the other hand, the electronic properties of bilayer WTe_2 remain relatively unexplored, apart from recent transport measurements[25] and first-principles calculations[23] that showed a semiconductor (semimetal) state with a tiny bandgap (band overlap), of only a few millielectronvolts. Because monolayer WTe_2 has a Dirac fermion at each Q (Q′) point in the Brillouin zone[23,25] (Extended Data Fig. 1), bilayer WTe_2 can be understood as having a pair of coupled Dirac fermions (one from each layer). The presence of Dirac fermions suggests large Berry curvatures if relevant crystalline symmetries are broken[1]. What makes the

[1]Department of Physics, Massachusetts Institute of Technology, Cambridge, MA, USA. [2]Department of Physics, National Cheng Kung University, Tainan, Taiwan. [3]Shenzhen Institute for Quantum Science and Engineering and Department of Physics, Southern University of Science and Technology, Shenzhen, China. [4]Shenzhen Key Laboratory of Quantum Science and Engineering, Shenzhen, China. [5]School of Physics, Southeast University, Nanjing, China. [6]Department of Physics, National University of Singapore, Singapore, Singapore. [7]Centre for Advanced 2D Materials and Graphene Research Centre, National University of Singapore, Singapore, Singapore. [8]Department of Physics, Harvard University, Cambridge, MA, USA. [9]Department of Chemistry, Princeton University, Princeton, NJ, USA. [10]National Institute for Materials Science, Tsukuba, Japan. [11]John A. Paulson School of Engineering and Applied Sciences, Harvard University, Cambridge, MA, USA. [12]Institute of Physics, Academia Sinica, Taipei, Taiwan. [13]These authors contributed equally: Qiong Ma, Su-Yang Xu, Huitao Shen. *e-mail: gedik@mit.edu; pjarillo@mit.edu

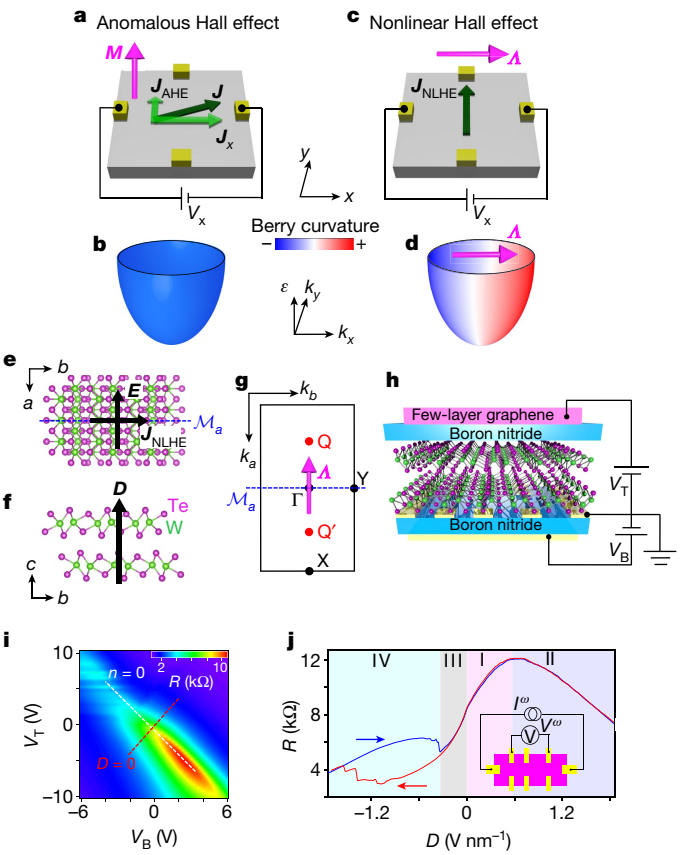

Fig. 1 | Crystal structure and basic characterization of bilayer WTe_2. **a**, Illustration of the anomalous Hall effect in a magnetic metal. $\boldsymbol{M}$ is the magnetization, $\boldsymbol{J}_{AHE}$ is the anomalous Hall current, J_x and V_x are the current and voltage, respectively, along the x direction, $\boldsymbol{J} = J_x + \boldsymbol{J}_{AHE}$ is the total current, the grey box represents the sample and the yellow squares represent the metal contacts. **b**, Schematic band structure (shape of the surface) and Berry curvature (colour scale) of a simple magnetic metal. The anomalous Hall conductivity arises from the momentum-integrated Berry curvature, which requires the breaking of time-reversal symmetry. **c**, Illustration of the nonlinear Hall effect. Because of the in-plane Berry-curvature dipole $\boldsymbol{\Lambda}$, an electrical bias parallel to $\boldsymbol{\Lambda}$ leads to a nonlinear Hall current ($\boldsymbol{J}_{NLHE}$). The linear longitudinal current J_x for conductors is not shown. **d**, Schematic distributions of the band structure and Berry curvature of a wide class of non-magnetic, inversion-symmetry-breaking quantum materials with non-zero $\boldsymbol{\Lambda}$. $\boldsymbol{\Lambda}$ originates from the segregation of positive and negative Berry curvature in k space, which does not necessarily break time-reversal symmetry. **e**, **f**, Top (**e**) and side (**f**) views of the crystal structure of bilayer WTe_2. $\boldsymbol{E}$ and $\boldsymbol{D}$ are the applied in-plane electric field and out-of-plane displacement field, respectively. The only crystalline symmetry is the mirror plane $\mathcal{M}_a$. Because of $\mathcal{M}_a$, $\boldsymbol{\Lambda}$ (a pseudovector) must be parallel to a in bilayer WTe_2 and thus an external electric field along a can lead to a nonlinear Hall voltage along b (see **c**). **g**, The first Brillouin zone, with important momenta shown in red. The pink arrow represents $\boldsymbol{\Lambda}$ in bilayer WTe_2. **h**, Schematic of an encapsulated, dual-gated, bilayer WTe_2 device. **i**, The four-probe longitudinal resistance R (colour scale) as a function of the top (V_T) and bottom (V_B) gate voltage at $T = 10$ K. The white and red dashed lines correspond to charge neutrality ($n = 0$) and zero displacement field ($D = 0$), respectively. **j**, The four-probe resistance R at $n = 0$ as a function of D (along the white dashed line in **i**). The blue and red curves correspond to forward and backward displacement field sweeps, respectively (as indicated by the arrows). The four regimes (I–IV) of the resistance are labelled. The resistance behaviour in these four regimes is described in Methods section 'Four-probe linear transport data'. The inset shows a schematic of the geometry for the transport measurements. I^{ω} and V^{ω} represent the current and voltage, respectively, at frequency ω.

electronic structure of the bilayer more unusual is its very low crystalline symmetry (Fig. 1e, f)[24,30]. Whereas monolayer WTe_2 is (approximately) inversion-symmetric[12,23], inversion symmetry is broken in bilayer WTe_2 (Fig. 1e, f)[24,30] because of the stacking arrangement, in contrast to hexagonal transition-metal dichalcogenides. The only crystalline symmetry for bilayer WTe_2 is the mirror plane $\mathcal{M}_a$ (Fig. 1e). Because of $\mathcal{M}_a$, $\boldsymbol{\Lambda}$ (a pseudovector) has to be parallel to the a axis (Fig. 1g). Therefore, as per the schematic in Fig. 1c, a nonlinear Hall voltage is expected to appear along the b axis in response to an external electric field along a (Fig. 1e).

We fabricated high-quality, encapsulated, dual-gated, bilayer WTe_2 devices (Fig. 1h), in which we can independently control the charge density n and the out-of-plane electrical displacement field $\boldsymbol{D}$. To optimize the devices for testing the nonlinear Hall effect, we selected flakes with long, straight edges and aligned the contacts along the straight edges. We start by studying the four-probe resistance of bilayer WTe_2. We find that this resistance is strongly asymmetric about $D = 0$ and exhibits ferroelectric switching[30] (Fig. 1i, j; Methods). The asymmetric resistance profile and the ferroelectric switching are both evidence for the low-symmetry nature of bilayer WTe_2 (Supplementary Information section II.4), in agreement with previous studies[24]. We also measured the mid-infrared circular photogalvanic effect (Fig. 2b, c), which confirms the inversion-symmetry-breaking nature of the bilayer and enabled us to determine the crystalline axes (Fig. 2a; Methods).

We now explore the nonlinear Hall effect in bilayer WTe_2. Phenomenologically, the nonlinear Hall effect can be described as $V^{NLHE}_{\alpha\beta\beta} \propto E_\beta E_\beta$, where E is the external electric field, α and β are the in-plane spatial directions ($\alpha \perp \beta$ for the Hall effect), and $V^{NLHE}_{\alpha\beta\beta}$ is the nonlinear Hall voltage along α in response to the external electric field along β. Hence, an a.c. electric field with frequency ω should[10] generate a voltage with double frequency $V^{2\omega}$, which can be measured directly by a lock-in amplifier in a phase-sensitive way. We study the qualitative behaviour of $V^{2\omega}$ at $T = 50$ K. By keeping the a.c. excitation current I^{ω} parallel to a, we test the longitudinal and transverse $V^{2\omega}$ ($V^{2\omega}_{aaa}$ and $V^{2\omega}_{baa}$, respectively; Fig. 2d). We observe a clear $V^{2\omega}_{baa}$ response between electrodes 3 and 4, which dominates the longitudinal response between electrodes 1 and 3 and electrodes 1 and 5. Moreover, $V^{2\omega}_{baa}$ exhibits a clear quadratic current–voltage (I–V) characteristic, which, combined with the 2ω frequency, establishes its second-order nature. In addition, the $V^{2\omega}_{baa}$ signal depends strongly on the gate voltage (Fig. 2e), whereas the quadratic $I-V$ characteristic is robust at all gate voltages.

We then perform systematic measurements at $T = 10$ K (Fig. 3). The gate map of $V^{2\omega}_{baa}$ (Fig. 3a) demonstrates a strong dependence on both n and $\boldsymbol{D}$. The black dashed line in Fig. 3a tracks the top and bottom gate voltages (V_T, V_B) that corresponding to the maximum of the resistance (Fig. 1i) at every value of D (Supplementary Information section II.2). We observe the following features in Fig. 3a. First, at $D = 0$, $V^{2\omega}_{baa}$ has the same sign on the opposite sides of the resistance peak (along the n axis). Upon further hole doping, the sign is reversed. Second, by applying a sufficiently large positive displacement field ($D > 0$), an additional sharp blue feature emerges very close to charge neutrality ($n = 0$) in between the two red features. In Fig. 3b, we compare the n dependence of $V^{2\omega}_{baa}$ and of the resistance along the green dashed line in Fig. 3a. The resistance is closely related to properties derived from the energy–momentum ($\varepsilon-k$) dispersion (such as the effective mass and the Fermi velocity) and to the defect scattering time τ. Therefore, the typical ambipolar behaviour that we observe demonstrates that the above properties evolve smoothly as a function of n. On the other hand, $V^{2\omega}_{baa}$ exhibits multiple sign reversals along the same trajectory. This contrasting behaviour reveals a distinct physical origin for $V^{2\omega}_{baa}$, beyond the $\varepsilon-k$ dispersion properties and τ: $V^{2\omega}_{baa}$ arises from a property whose sign depends sensitively on the chemical potential ε_F. We show the temperature dependence of $V^{2\omega}_{baa}$ and of the resistance in Extended Data Fig. 3. In Fig. 3c, we show the measured $V^{2\omega}$ signals between many combinations of electrodes. Irrespective of the choice of electrodes, the transverse response dominates the longitudinal response and all $V^{2\omega}_{baa}$ data collapse onto a single curve (Fig. 3c). These measurements clearly demonstrate the Hall nature of the $V^{2\omega}$ signals. Our data in Fig. 3c demonstrate a Hall angle of around 90° for the nonlinear response (Fig. 3d).

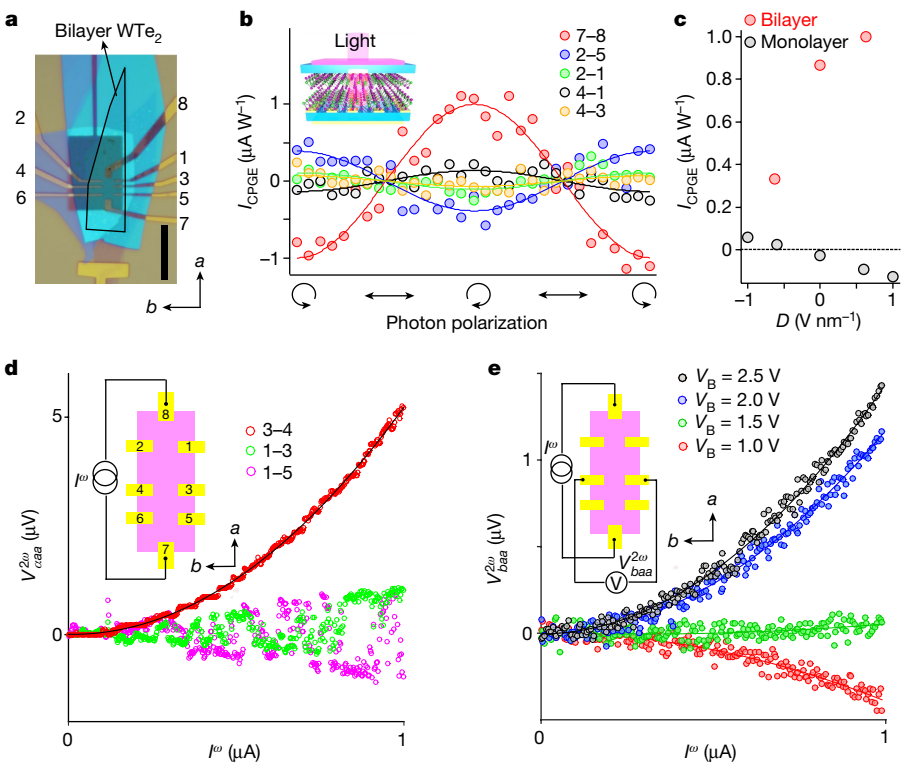

Fig. 2 | Circular photocurrents and nonlinear transport in bilayer WTe_2. **a**, Optical image of our WTe_2 device, with the electrodes numbered. The black lines trace the encapsulated bilayer WTe_2 flake. The crystalline directions determined from the circular photogalvanic effect (CPGE) are noted. Scale bar, 15 μm. **b**, Polarization-dependent photocurrents I_{CPGE} between different electrodes (see legend). We shine mid-infrared light (photon energy of approximately 120 meV) under normal incidence onto the sample and collect the photocurrent without applying any electrical bias (see inset). The solid lines are fits using a cosine function. **c**, I_{CPGE} of bilayer and monolayer WTe_2 samples as a function of D under similar conditions (device geometry, flake size, temperature, and so on). **d**, By flowing an a.c. current ($I^{\omega}||a$; frequency $\omega = 177.77$ Hz) between electrodes 7 and 8, we detect the nonlinear voltages $V^{2\omega}_{\alpha aa}$ along the longitudinal ($\alpha = a$; green and purple) and transverse ($\alpha = b$; red) directions. **e**, $V^{2\omega}_{baa}$ ($V^{2\omega}$ along b in response to $I^{\omega}||a$ at $V_T = -4.5$ V and different V_B). The solid lines in **d** and **e** are quadratic fits to the data. Data in **b**–**d** were collected at $T = 50$ K; data in **e** were collected at $T = 100$ K.

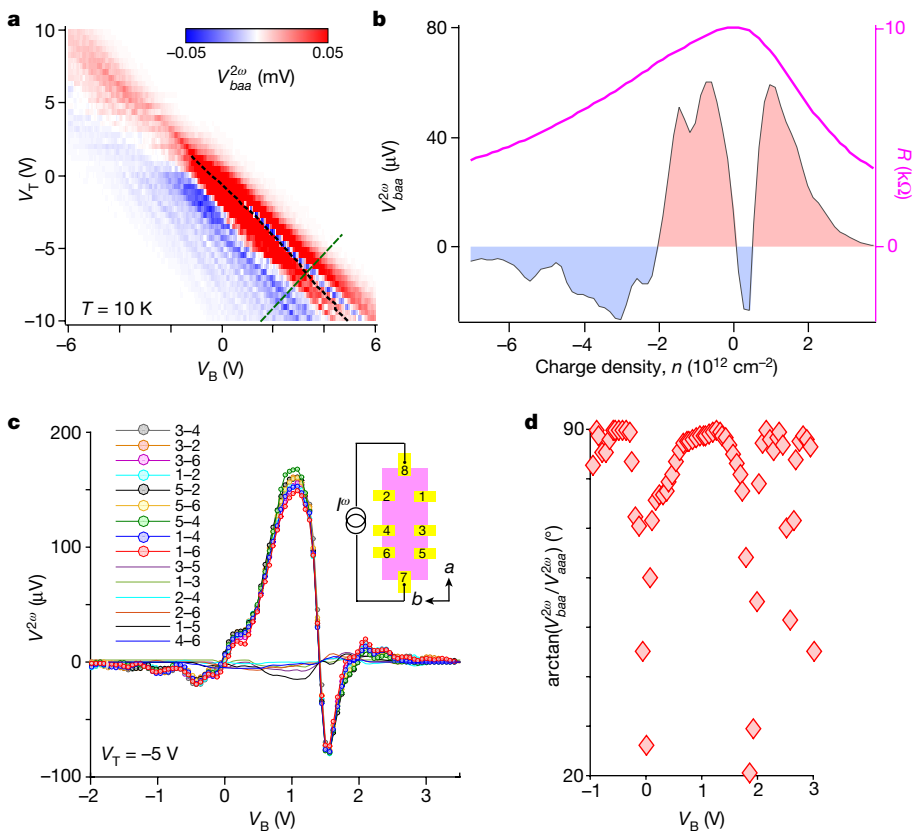

Fig. 3 | Systematic studies of the nonlinear Hall effect in bilayer WTe_2. **a**, Gate map of $V^{2\omega}_{baa}$ at $T = 10$ K. A current $I^{\omega} = 1$ μA is applied for all gate voltages. The black dashed line traces the (V_T, V_B) that correspond to the maximum resistance (Fig. 1i) at every D (see Supplementary Information section II.2). The green dashed line denotes a trajectory along which n is varied at constant D. **b**, $V^{2\omega}_{baa}$ (left, black line) and R (right, magenta line) as a function of n along the green dashed line in **a**. The blue (red) shading highlights negative (positive) $V^{2\omega}_{baa}$. **c**, $V^{2\omega}$ measured between many combinations of electrodes while keeping $I^{\omega}||a$ (see inset). Transverse (longitudinal) signals are shown by lines with (without) symbols. **d**, The nonlinear Hall angle $\arctan(V^{2\omega}_{baa}/V^{2\omega}_{aaa})$ between the transverse ($V^{2\omega}_{baa}$) and longitudinal ($V^{2\omega}_{aaa}$) Hall voltages, determined from the data in **c**.

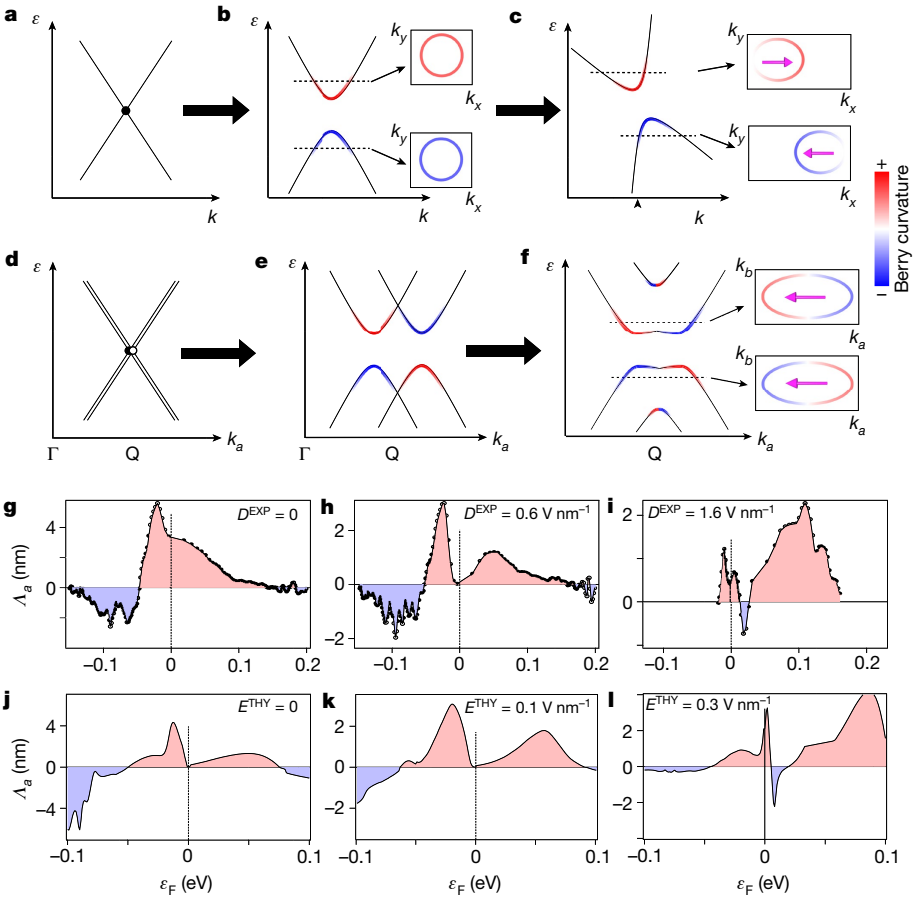

Fig. 4 | Large Berry-curvature dipole arising from layer-polarized Dirac fermions in bilayer WTe_2. **a**, A massless Dirac fermion (solid lines and black filled circle) does not have any Berry curvature (colour scale). **b**, Opening an energy gap at the Dirac point (the black filled circle) by breaking inversion symmetry leads to large Berry curvature near the edges of the gap. **c**, Tilting the Dirac cone allows the states at the Fermi level to have different Berry curvatures and different $\partial\varepsilon/\partial k_\alpha$, leading to non-zero $\boldsymbol{\Lambda}$, with opposite signs for the conduction and valence bands (purple arrows; see equation (1) in Methods). **d**, In the absence of inter-layer and spin–orbit coupling, the Q point of bilayer WTe_2 features a pair of degenerate, massless Dirac fermions (one from each layer) of opposite chirality (filled and open circles). **e**, By turning on inter-layer coupling, the two Dirac fermions are gapped because of the explicit breaking of inversion symmetry due to the inter-layer coupling. For a gapped Dirac fermion, the conduction and valence bands have opposite Berry curvature. The sign of the Berry curvature depends on the chirality of the Dirac fermion. The two Dirac fermions are shifted with respect to each other. **f**, The inter-layer coupling opens up further gaps wherever the Dirac fermions cross. As a result, the left and right movers have opposite Berry curvature, which leads to large $\boldsymbol{\Lambda}$ (purple arrows; see equation (1) in Methods). $\boldsymbol{\Lambda}$ has the same sign for the conduction and valence bands, which is a unique signature of asymmetrically coupled Dirac fermions in bilayer WTe_2. In **a**–**f**, the main panels show schematics of the band dispersion (solid lines) and the distribution of Berry curvature (colour scale); the dashed lines highlight representative energies. The insets of **b**, **c**, **f** show schematics of constant-energy contours (shape of the contours) and the Berry-curvature distribution (colour scale) at the energies marked by the dashed lines in the main panels. **g**–**i**, Experimentally obtained Berry-curvature dipole Λ_a at three different experimental displacement fields D^{EXP}. We determine Λ_a as a function of n at a given D from the $V_{baa}^{2\omega}$ data in Fig. 3a and then relate n to the chemical potential ε_F using first-principles calculations (see Supplementary Information section VII for details). **j**–**l**, Theoretically calculated Λ_a at three different theoretical displacement fields D^{THY}. The theoretically applied electric field E^{THY} is related to the displacement field by $D^{THY} = \varepsilon^{WeT2}E^{THY}$, where ε^{WeT2} is the relative dielectric constant of bilayer WTe_2 along the out-of-plane direction.

We highlight here the key data, including the clear observation of the nonlinear Hall voltage $V_{baa}^{2\omega}$, its dominance over the longitudinal response, its gate dependence and its consistency across many combinations of electrodes. These data are crucial for excluding various extrinsic effects. For instance, an accidental diode at the contact–sample interface could lead to a rectification effect. For any extrinsic signal, the Hall (transverse) signal should not dominate over the longitudinal signal. Moreover, extrinsic signals can be ruled out by the consistent data for many combinations of electrodes. See Supplementary Information section VIII for a discussion on how extrinsic effects are considered and excluded. We now consider the $\boldsymbol{\Lambda}$-induced nonlinear Hall effect as a possible origin for our data. Our observation of $V_{baa}^{2\omega}$ is consistent with the general symmetry expectation for the $\boldsymbol{\Lambda}$ effect in bilayer WTe_2 (Fig. 1e). To confirm this origin more directly, we take advantage of the additional tuning parameters provided by the dual gating. In particular, our $V_{baa}^{2\omega}$ data exhibit a distinct gate dependence, consisting of a strong dependence on $\boldsymbol{D}$ and multiple sign reversals as a function of ε_F. These experimental features over a large parameter space provide information about the physical origin of the nonlinear Hall signals that we observe that may be compared directly with the Berry-curvature behaviour in bilayer WTe_2. In Fig. 4a–f, we provide an illustration of the mechanism underlying the unusual $\boldsymbol{\Lambda}$ in bilayer WTe_2 (see Methods for a detailed description). This illustration allows us to understand why a large $\boldsymbol{\Lambda}$ can form as a result of asymmetrically coupled Dirac fermions, and some of its key features at different energies.

Finally, we determine the Berry-curvature dipole Λ_a from the $V_{baa}^{2\omega}$ data (Fig. 4g–i; Supplementary Information section VII) and compare directly with the results of first-principles calculations. At $D = 0$ and $D = 0.6$ V nm^{-1} (Fig. 4g, h), Λ_a has a positive peak on either side of $\varepsilon_F = 0$; further away from $\varepsilon_F = 0$, Λ_a becomes negative. These behaviours are consistent with the calculations shown in Fig. 4j, k.

At $D = 1.6\ \mathrm{V\ nm^{-1}}$, a sharp, negative feature appears in the data near $\varepsilon_F = 0$ (Fig. 4i), which is also captured by the theory (Fig. 4l). In fact, the calculations show two sharp peaks immediately next to each other; the positive one merges with a broader feature of the same sign. The agreement between data and first-principles calculations provides compelling evidence for our experimental observation of the $\boldsymbol{\Lambda}$-induced nonlinear Hall effect.

Our results demonstrate a new type of Hall effect. The spin Hall effect been observed previously under time-reversal-symmetric conditions; however, it generates only a spin voltage, not an electrical voltage. By contrast, the nonlinear Hall effect is an electrical Hall effect in a non-magnetic material and in the absence of a magnetic field. We also highlight its importance as a Berry-curvature probe: whereas the anomalous Hall effect has been used to measure the Berry curvature of magnetic metals and semimetals, a similar probe for their non-magnetic counterparts has been lacking. Signals of the nonlinear Hall effect always correspond to $\boldsymbol{\Lambda}$ at the Fermi level, irrespective of the details of the band structure (such as the absence or presence of spin–orbit coupling and the number of Fermi surfaces); to obtain $\boldsymbol{\Lambda}$ from the signal of the nonlinear Hall effect, only τ is further needed, which can be obtained from standard electrical transport measurements. These characteristics highlight the nonlinear Hall effect as a powerful and universal probe of the Berry curvature in non-magnetic quantum metals and semimetals. This is complementary to previous optoelectronic approaches in wide-gap semiconductors with valley selection rules[1,31]. Moreover, the nonlinear Hall effect reveals that the distribution of the Berry curvature in k space (Berry-curvature dipoles, quadruples, and so on) modifies the electrical, thermoelectric, optical, plasmonic and other key properties of quantum materials. Many ordered states (including charge-density waves and superconductivity) manifest as the breaking of a particular symmetry for the electrons near the Fermi level. Because the nonlinear transport demonstrated here combines sensitivity to symmetry, as in nonlinear optics, and sensitivity to Fermi-energy physics, as in regular transport, it may be used to probe order parameters of other broken-symmetry states[32,33]. Finally, the responsivity of our WTe_2 device, defined as the ratio between the nonlinear output voltage and the input power, reaches a value of $10^4\ \mathrm{V\ W^{-1}}$ (see Supplementary Information section IX for discussion). This large responsivity highlights the potential of using the intrinsic quantum properties of homogenous quantum materials for nonlinear applications, including frequency-doubling and rectification. The generalization to gigahertz or terahertz frequencies might be useful for next-generation wireless technologies.

Online content

Any methods, additional references, Nature Research reporting summaries, source data, statements of data availability and associated accession codes are available at https://doi.org/10.1038/s41586-018-0807-6.

Received: 10 July 2018; Accepted: 14 November 2018;
Published online 17 December 2018.

1. Xiao, D., Chang, M.-C. & Niu, Q. Berry phase effects on electronic properties. *Rev. Mod. Phys.* **82**, 1959–2007 (2010).
2. Nagaosa, N., Sinova, J., Onoda, S., MacDonald, A. & Ong, N. P. Anomalous Hall effect. *Rev. Mod. Phys.* **82**, 1539–1592 (2010).
3. Chang, C.-Z. et al. Experimental observation of the quantum anomalous Hall effect in a magnetic topological insulator. *Science* **340**, 167–170 (2013).
4. Binz, B. & Vishwanath, A. Chirality induced anomalous-Hall effect in helical spin crystals. *Physica B* **403**, 1336–1340 (2008).
5. Nakatsuji, S., Kiyohara, N. & Higo, T. Large anomalous Hall effect in a non-collinear antiferromagnet at room temperature. *Nature* **527**, 212–215 (2015).
6. Yasuda, K. et al. Geometric Hall effects in topological insulator heterostructures. *Nat. Phys.* **12**, 555–559 (2016).
7. Liu, E. et al. Giant anomalous Hall effect in a ferromagnetic kagome-lattice semimetal. *Nat. Phys.* **14**, 1125–1131 (2018).
8. Deyo, E., Golub, L., Ivchenko, E. & Spivak, B. Semiclassical theory of the photogalvanic effect in non-centrosymmetric systems. Preprint at https://arxiv.org/abs/0904.1917 (2009).
9. Moore, J. E. & Orenstein, J. Confinement-induced Berry phase and helicity-dependent photocurrents. *Phys. Rev. Lett.* **105**, 026805 (2010).
10. Sodemann, I. & Fu, L. Quantum nonlinear Hall effect induced by Berry curvature dipole in time-reversal invariant materials. *Phys. Rev. Lett.* **115**, 216806 (2015).
11. Lee, J., Wang, Z., Xie, H., Mak, K. F. & Shan, J. Valley magnetoelectricity in single-layer MoS_2. *Nat. Mater.* **16**, 887–891 (2017).
12. Xu, S.-Y. et al. Electrically switchable Berry curvature dipole in the monolayer topological insulator WTe_2. *Nat. Phys.* **14**, 900–906 (2018).
13. Low, T., Jiang, Y. & Guinea, F. Topological currents in black phosphorus with broken inversion symmetry. *Phys. Rev. B* **92**, 235447 (2015).
14. Morimoto, T. & Nagaosa, N. Chiral anomaly and giant magnetochiral anisotropy in noncentrosymmetric Weyl semimetals. *Phys. Rev. Lett.* **117**, 146603 (2016).
15. Zhang, Y., Sun, Y. & Yan, B. The Berry curvature dipole in Weyl semimetal materials: an *ab initio* study. *Phys. Rev. B* **97**, 041101(R) (2018).
16. Tsirkin, S. S., Puente, P. A. & Souza, I. Gyrotropic effects in trigonal tellurium studied from first principles. *Phys. Rev. B* **97**, 035158 (2018).
17. Zhang, Y., Brink, J. V. d., Felser, C. & Yan, B. Electrically tuneable nonlinear anomalous Hall effect in two-dimensional transition-metal dichalcogenides WTe_2 and $MoTe_2$. *2D Materials* **5**, 044001 (2018).
18. You, J.-S., Fang, S., Xu, S.-Y., Kaxiras, E. & Low, T. The Berry curvature dipole current in transition metal dichalcogenides family. *Phys. Rev. B* **98**, 121109(R) (2018).
19. Shi, L.-k. & Song, J. C. W. Berry curvature switch and magneto-electric effect in WTe_2 monolayer. Preprint at https://arxiv.org/abs/1805.00939 (2018).
20. Facio, J. I. et al. Giant enhancement of Berry-dipole at topological phase transitions in BiTeI. Preprint at https://arxiv.org/abs/1805.02680 (2018).
21. Ali, M. N. et al. Large, non-saturating magnetoresistance in WTe_2. *Nature* **514**, 205–208 (2014).
22. Soluyanov, A. et al. Type-II Weyl semimetals. *Nature* **527**, 495–498 (2015).
23. Qian, X., Liu, J., Fu, L. & Li, J. Quantum spin Hall effect in two-dimensional transition metal dichalcogenides. *Science* **346**, 1344–1347 (2014).
24. MacNeill, D. et al. Control of spin-orbit torques through crystal symmetry in WTe_2/ferromagnet bilayers. *Nat. Phys.* **13**, 300–305 (2016).
25. Fei, Z. et al. Edge conduction in monolayer WTe_2. *Nat. Phys.* **13**, 677–682 (2017).
26. Tang, S. et al. Quantum spin Hall state in monolayer 1T′-WTe_2. *Nat. Phys.* **13**, 683–687 (2017).
27. Wu, S. et al. Observation of the quantum spin Hall effect up to 100 Kelvin in a monolayer crystal. *Science* **359**, 76–79 (2018).
28. Fatemi, V. et al. Electrically tunable low density superconductivity in a monolayer topological insulator. *Science* **362**, 926–929 (2018).
29. Sajadi, E. et al. Gate-induced superconductivity in a monolayer topological insulator. *Science* **362** 922–925 (2018).
30. Fei, Z. et al. Ferroelectric switching of a two-dimensional metal. *Nature* **560**, 336–339 (2018).
31. Mak, K. F., McGill, K. L., Park, J. & McEuen, P. L. The valley Hall effect in MoS_2 transistors. *Science* **344**, 1489–1492 (2014).
32. Qin, F. et al. Superconductivity in a chiral nanotube. *Nat. Commun.* **8**, 14465 (2017).
33. Harter, J., Zhao, Z., Yan, J.-Q., Mandrus, D. & Hsieh, D. A parity-breaking electronic nematic phase transition in the spin-orbit coupled metal $Cd_2Re_2O_7$. *Science* **356**, 295–299 (2017).

Acknowledgements We thank J. Checkelsky, F. Qin, Y. Iwasa, J.-S. You and I. Sodemann for discussions. Work in the PJH group was supported partly by the Center for Excitonics, an Energy Frontier Research Center funded by the US Department of Energy (DOE), Office of Science, Office of Basic Energy Sciences (BES) under award number DESC0001088 (fabrication and measurement) and partly through AFOSR grant FA9550-16-1-0382 (data analysis), and by the Gordon and Betty Moore Foundation's EPiQS Initiative through grant GBMF4541 to P.J.-H. This work made use of the Materials Research Science and Engineering Center Shared Experimental Facilities supported by the National Science Foundation (NSF; grant number DMR-0819762). N.G. and S.-Y.X. acknowledge support from DOE, BES DMSE (data taking and analysis), the Gordon and Betty Moore Foundations EPiQS Initiative through grant GBMF4540 (manuscript writing) and NSF grant number DMR-1809815 (modelling). The WTe_2 crystal growth performed at Princeton University was supported by NSF MRSEC grant DMR-1420541 (Q.D.G. and R.J.C.). Z.D. and H.-Z.L. were supported by the Guangdong Innovative and Entrepreneurial Research Team Program (2016ZT06D348), the National Key R&D Program (2016YFA0301700), the National Natural Science Foundation of China (11574127), and the Science, Technology, and Innovation Commission of Shenzhen Municipality (ZDSYS20170303165926217 and JCYJ20170412152620376). K.W. and T.T. acknowledge support from the Elemental Strategy Initiative conducted by MEXT, Japan, JSPS KAKENHI grant numbers JP18K19136 and CREST (JPMJCR15F3), JST. H.S., L.F. and S.F. acknowledge support from NSF Science and Technology Center for Integrated Quantum Materials grant DMR-1231319 (theory for H.S. and L.F.; calculations for S.F.). H.L. acknowledges Academia Sinica, Taiwan, for support under Innovative Materials and Analysis Technology Exploration (AS-iMATE-107-11). T.-R.C. was supported by the Young Scholar Fellowship Program by Ministry of Science and Technology (MOST) in Taiwan, under MOST Grant for the Columbus Program MOST107-2636-M-006-004, National Cheng Kung University, Taiwan, and National Center for Theoretical Sciences (NCTS), Taiwan. E.K. acknowledges support by ARO MURI Award W911NF-14-0247. The computational work at Harvard University was performed on the

Odyssey cluster, which is supported by the FAS Division of Science, Research Computing Group.

Reviewer information *Nature* thanks J. van den Brink and the other anonymous reviewer(s) for their contribution to the peer review of this work.

Author contributions P.J.-H. and N.G. supervised the project. S.-Y.X. and Q.M. conceived the experiment, performed the photocurrent measurements and analysed the data. Q.M., S.-Y.X. and D.M. performed the transport measurements with help from V.F., and all performed data analysis and discussed the results. A.M.M.V., Q.M., D.M., S.W. and V.F. fabricated the devices. T.-R.C., C.-H.H. and S.F. calculated the first-principles band structures and the Berry-curvature dipole in bilayer WTe_2 under the supervision of E.K. and H.L. H.S., S.-Y.X. and Z.D. performed the theoretical modelling and analyses under the supervision of H.-Z.L. and L.F. Q.D.G. and R.J.C. grew the bulk WTe_2 single crystals. K.W. and T.T. grew the bulk hexagonal boron nitride single crystals. S.-Y.X., Q.M., N.G. and P.J.-H. wrote the manuscript, with input from all authors.

Competing interests The authors declare no competing interests.

Additional information

Extended data is available for this paper at https://doi.org/10.1038/s41586-018-0807-6.
Supplementary information is available for this paper at https://doi.org/10.1038/s41586-018-0807-6.
Reprints and permissions information is available at http://www.nature.com/reprints.
Correspondence and requests for materials should be addressed to N.G. or P.J.

METHODS

Sample fabrication. High-quality bulk WTe_2 crystals[34] were grown using a previously described method[21]. Our fabrication of the dual-gated bilayer WTe_2 devices consists of two phases. Phase I was done under ambient conditions: local bottom PdAu or graphite gates were first defined on standard Si/SiO_2 substrates. A suitable hexagonal boron nitride (hBN) flake (roughly 10–20 nm thick) was exfoliated onto a separate Si/SiO_2 substrate, picked up using a polymer-based dry transfer technique and placed onto the pre-patterned local bottom gate. Electrical contacts (PdAu, about 20 nm thick) were deposited onto the bottom hBN flake with *e*-beam lithography and metal deposition. Alternatively (for the device in Supplementary Information section II.3), patterned graphene fingers were transferred on top of the hBN as the bottom electrodes. Phase II was done fully inside a glovebox with an argon environment. Bilayer WTe_2 flakes were exfoliated from a bulk crystal onto a Si/SiO_2 chip. Flakes with long, straight edges (an indication of the crystalline axis[35]) were selected and contacts were aligned along the straight edges. Few-layer graphene, hBN (about 10–20 nm thick) and bilayer WTe_2 were sequentially picked up and then transferred onto the local bottom gate/hBN/contact substrate. Extended leads connecting the top-gate graphene to wire bonding pads were pre-made together with the metal contacts in phase I. In such a dual-gated device, the charge density is $n = \varepsilon_0 \varepsilon^{\mathrm{hBN}}(V_{\mathrm{T}}/h_{\mathrm{T}} + V_{\mathrm{B}}/h_{\mathrm{B}})/e$, where V_{T} (V_{B}) is the voltage of the top (bottom) gate, $\varepsilon_0 = 8.85 \times 10^{-12}\ \mathrm{F\,m^{-1}}$ is the vacuum permittivity, $h_{\mathrm{T}} = 16$ nm ($h_{\mathrm{B}} = 10$ nm) is the thickness of the top (bottom) hBN layer of the device and $\varepsilon^{\mathrm{hBN}} \approx 3$ is the relative dielectric constant of the hBN layers. The displacement field is determined[36] by $D = \varepsilon^{\mathrm{hBN}}(V_{\mathrm{B}}/h_{\mathrm{B}} - V_{\mathrm{T}}/h_{\mathrm{T}})/2$.

Transport measurements. Electrical transport was measured in a He-3 cryostat. The top and bottom gate voltages were applied through two Keithley 2400 SourceMeters. First- and second-harmonic signals were collected by standard lock-in techniques (Stanford Research Systems Model SR830) with excitation frequencies of 10–200 Hz. Three frequencies (17.777 Hz, 77.77 Hz and 177.77 Hz) were tested, yielding consistent data (Supplementary Information section II.1). These frequencies correspond to $\omega\tau \to 0$ and $\hbar\omega \ll \varepsilon_{\mathrm{F}}, E_{\mathrm{g}}$, where τ is the relaxation time, ε_{F} is the chemical potential and E_{g} is the typical bandgap. These conditions ensure that our experiments are within the semi-classical Drude limit[10], in which the indirect, intra-band optical processes are expected to be weak[37]. The phase of the first-harmonic (second-harmonic) signal was approximately 0° (±90°), consistent with the expected values for first- and second-order responses[32,38,39]. In the presence of an a.c. excitation current $I^{\omega} = I_0 \sin(\omega t)$, the second-order voltage is $V^{\mathrm{second-order}} \propto [I_0 \sin(\omega t)]^2 = I_0^2[1 + \sin(2\omega t - \pi/2)]/2$, directly revealing the phase difference between the first- and second-harmonic signals. This equation also shows that $V^{\mathrm{second\text{-}order}}$ always consists of a second-harmonic component and a d.c. component. The coexistence of second-harmonic and d.c. components is a generic property for various second-order transport effects, including the nonlinear Hall effect[10], the non-reciprocal current with magnetic fields[32,38,39], the spin-torque in magnetic materials and hetereostructures[24,40–43], and other rectification effects on diodes and other external junctions (Supplementary Information section VIII). Similarly to measurements of the reciprocal current and magnetic spin-torque[24,32,38–43], we focus on the second-harmonic signals because that allows us to use the lock-in technique, which greatly enhances the measurement sensitivity and precision.

Four-probe linear transport data. In Fig. 1j, we plot the resistance at charge neutrality as a function of D: from $D = 0$ to $D > 0$, the resistance increases in regime I and then decreases in regime II. By contrast, from $D = 0$ to $D < 0$, the resistance decreases in regime III and exhibits large hysteresis in regime IV. The strong asymmetry that we observe in the resistance data in bilayer WTe_2 arises directly from the lack of any symmetry that relates c to $-c$ (Extended Data Fig. 1; Supplementary Information section II.4). This property of bilayer WTe_2 is not present in other known two-dimensional materials, such as bilayer graphene, bilayer hexagonal transition-metal dichalcogenides and monolayer WTe_2. The large hysteresis in regime IV suggests D-field-driven ferroelectric switching[30].

Mid-infrared scanning photocurrent microscopy. The laser source is a temperature-stabilized CO_2 laser (wavelength $\lambda = 10.6$ μm; photon energy $\hbar\omega = 120$ meV). A focused beam spot (beam waist of approximately 25 μm) is scanned (using a two-axis piezo-controlled scanning mirror) over the entire sample and the current is recorded at the same time to form a two-dimensional map of the photocurrent as a function of spatial position. Reflected light from the sample is collected to form a simultaneous reflection image of the sample. The absolute location of the photo-induced signal is therefore found by comparing the photocurrent map to the reflection image. The light polarization is modulated by a rotatable quarter-wave plate. As shown in Fig. 2c, the CPGE in bilayer WTe_2 is about an order of magnitude stronger than in monolayer WTe_2, which clearly demonstrates the strong inversion-symmetry breaking of the bilayer. Moreover, the D-field dependence of the CPGE is asymmetric about $D = 0$ in the bilayer but roughly symmetric in the monolayer (Fig. 2c), consistent with the resistance behaviour (Fig. 1i, j). Furthermore, the clear directional dependence of the CPGE allows us to determine the crystalline axes (Supplementary Information section IV). As shown in Fig. 2b, the direction connecting electrodes 7 and 8 roughly corresponds to the crystalline a axis, which is consistent with the shape of the bilayer flake (Fig. 2a).

Mechanism for the Berry-curvature dipole in bilayer WTe_2. Here we elucidate the mechanism underlying the unusual $\boldsymbol{\Lambda}$ in bilayer WTe_2, to understand why a large $\boldsymbol{\Lambda}$ can form from asymmetrically coupled Dirac fermions, and some of its key features at different energies.

As a starting point, a massless Dirac fermion (as in graphene) has no Berry curvature (Fig. 4a). Opening an energy gap at the Dirac point by breaking inversion symmetry (as in gapped graphene or hexagonal transition-metal dichalcogenide monolayers) leads to large Berry curvature Ω near the gap edges[1,44] (Fig. 4b). However, $\boldsymbol{\Lambda}$ is still zero because Ω is uniform around the Fermi surface (Fig. 4b). To describe this mathematically, we write down the expression for $\boldsymbol{\Lambda}$[10]:

$$\Lambda_{\alpha} = -\frac{1}{\hbar}\int \delta(\varepsilon - \varepsilon_{\mathrm{F}})\frac{\partial \varepsilon}{\partial k_{\alpha}}\Omega(\boldsymbol{k})\mathrm{d}^2\boldsymbol{k} \tag{1}$$

where ε is the energy, $\boldsymbol{k}$ is the wavevector, ε_{F} is the chemical potential and $\partial\varepsilon/\partial k_{\alpha}$ is the band slope along α. This integral vanishes because Ω is constant whereas $\partial\varepsilon/\partial k_{\alpha}$ is equal but opposite on the opposite sides of the Fermi surface. Tilting the Dirac cone allows the left and right movers to have different Ω and different $\partial\varepsilon/\partial k_{\alpha}$ (Fig. 4c), leading to a non-zero $\boldsymbol{\Lambda}$. Importantly, for a single Dirac fermion, $\boldsymbol{\Lambda}$ is opposite for the conduction and valence bands (Fig. 4c, equation (1)).

We now consider bilayer WTe_2. In the absence of inter-layer and spin–orbit coupling, the Q point has a pair of decoupled, massless Dirac fermions of opposite chirality (one from each layer; Fig. 4d). In the presence of inter-layer coupling, the two Dirac fermions are gapped because of the explicit breaking of inversion symmetry due to inter-layer coupling (Fig. 4e). Inter-layer coupling also shifts the two Dirac fermions with respect to each other and opens up gaps wherever they cross (Fig. 4f). To capture the essential physics, we considered only the shift along momentum and ignored the shift along energy. As a result, the left and right movers have opposite Berry curvature (Fig. 4f). This relatively simple picture already captures some of the key features in our data. First, the asymmetrically coupled Dirac fermions lead to a large $\boldsymbol{\Lambda}$ along a, consistent with the observed nonlinear Hall voltage $V_{baa}^{2\omega}$. Second, $\boldsymbol{\Lambda}$ has the same sign for the conduction and valence bands immediately next to charge neutrality, consistent with the $V_{baa}^{2\omega}$ data at $D = 0$. In Supplementary Information sections V and VI, we consider the shift along energy, the inclusion of spin–orbit coupling and the effect of the D field. This analysis allows us to capture and understand other main features of the data, including the sign reversal at large hole doping and the appearance of the sharp blue feature at $D > 0$ in Fig. 3a, which arises from an anti-crossing (a massive Dirac fermion) between the lowest two conduction bands (green circle in Extended Data Fig. 2d; see Supplementary Information section V).

First-principles calculations. We performed first-principles band-structure calculations using the projector augmented wave method as implemented in the VASP package[45,46] within the generalized gradient approximation scheme. We used $11 \times 15 \times 1$ Monkhorst–Pack k-point meshes with an energy cut-off of 400 eV for slab calculations. The vacuum thickness was larger than 20 Å to ensure separation of the slabs. To correct the energy bandgaps, we also performed calculations with the Heyd–Scuseria–Ernzerhof hybrid functional[47,48]. We used W d and Te p orbitals to construct Wannier functions[49] without performing the procedure for maximizing localization. We calculated the Berry curvature of the nth band ($\Omega_n(\boldsymbol{k})$) in a two-dimensional system using the standard Kubo formula:

$$\Omega_n(\boldsymbol{k}) = i\sum_{n'\neq n}\frac{1}{(\varepsilon_{n'}-\varepsilon_n)^2}\left(\left\langle n'\left|\frac{\partial H}{\partial k_x}\right|n\right\rangle\left\langle n\left|\frac{\partial H}{\partial k_y}\right|n'\right\rangle - \left\langle n'\left|\frac{\partial H}{\partial k_y}\right|n\right\rangle\left\langle n\left|\frac{\partial H}{\partial k_x}\right|n'\right\rangle\right)$$

Our first-principles calculation considered 88 bands, which covers approximately ±6 eV from the Fermi energy. This ensures that we can reliably compute the Berry curvature of the low-energy state. A 501×501 k mesh was then used to compute $\boldsymbol{\Lambda}$ via

$$\Lambda_a = -\frac{1}{\hbar}\int \frac{\partial f_0(\mu, \boldsymbol{k})}{\partial k_{\alpha}}\Omega(\boldsymbol{k})\mathrm{d}^2\boldsymbol{k}$$

where μ is the chemical potential and $f_0(\mu, \boldsymbol{k})$ is the equilibrium distribution function.

Data availability

The data shown in the plots and that support the other findings of this study are available from the corresponding authors on reasonable request.

34. Mar, A., Jobic, S. & Ibers, J. A. Metal-metal vs tellurium-tellurium bonding in WTe_2 and its ternary variants $TaIrTe_4$ and $NbIrTe_4$. *J. Am. Chem. Soc.* **114**, 8963–8971 (1992).
35. Beams, R. et al. Characterization of few-layer 1T′ $MoTe_2$ by polarization-resolved second harmonic generation and Raman scattering. *ACS Nano* **10**, 9626–9636 (2016).
36. Taychatanapat, T. & Jarillo-Herrero, P. Electronic transport in dual-gated bilayer graphene at large displacement fields. *Phys. Rev. Lett.* **105**, 166601 (2010).
37. Golub, L. E. & Ivchenko, E. L. Circular and magnetoinduced photocurrents in Weyl semimetals. *Phys. Rev. B* **98**, 075305 (2018).
38. Ideue, T. et al. Bulk rectification effect in a polar semiconductor. *Nat. Phys.* **13**, 578–583 (2017).
39. Wakatsuki, R. et al. Nonreciprocal charge transport in noncentrosymmetric superconductors. *Sci. Adv.* **3**, e1602390 (2017).
40. Sinova, J., Valenzuela, S. O., Wunderlich, J., Back, C. & Jungwirth, T. Spin Hall effects. *Rev. Mod. Phys.* **87**, 1213–1260 (2015).
41. Kim, J. et al. Layer thickness dependence of the current-induced effective field vector in Ta|CoFeB|MgO. *Nat. Mater.* **12**, 240–245 (2013).
42. Garello, K. et al. Symmetry and magnitude of spin-orbit torques in ferromagnetic heterostructures. *Nat. Nanotechnol.* **8**, 587–593 (2013).
43. MacNeill, D. et al. Thickness dependence of spin-orbit torques generated by WTe_2. *Phys. Rev. B* **96**, 054450 (2017).
44. Yao, W., Xiao, D. & Niu, Q. Valley-dependent optoelectronics from inversion symmetry breaking. *Phys. Rev. B* **77**, 235406 (2008).
45. Perdew, J. P., Burke, K. & Ernzerhof, M. Generalized gradient approximation made simple. *Phys. Rev. Lett.* **77**, 3865–3868 (1996).
46. Kresse, G. & Furthmüller, J. Efficient iterative schemes for *ab initio* total-energy calculations using a plane-wave basis set. *Phys. Rev. B* **54**, 11169–11186 (1996).
47. Heyd, J., Scuseria, G. E. & Ernzerhof, M. Hybrid functionals based on a screened Coulomb potential. *J. Chem. Phys.* **118**, 8207–8215 (2003).
48. Zheng, F. et al. On the quantum spin Hall gap of monolayer 1T′-WTe_2. *Adv. Mater.* **28**, 4845–4851 (2016).
49. Souza, I., Marzari, N. & Vanderbilt, D. Maximally localized Wannier functions for entangled energy bands. *Phys. Rev. B* **65**, 035109 (2001).
50. Muechler, L., Alexandradinata, A., Neupert, T. & Car, R. Topological nonsymmorphic metals from band inversion. *Phys. Rev. X* **6**, 041069 (2016).

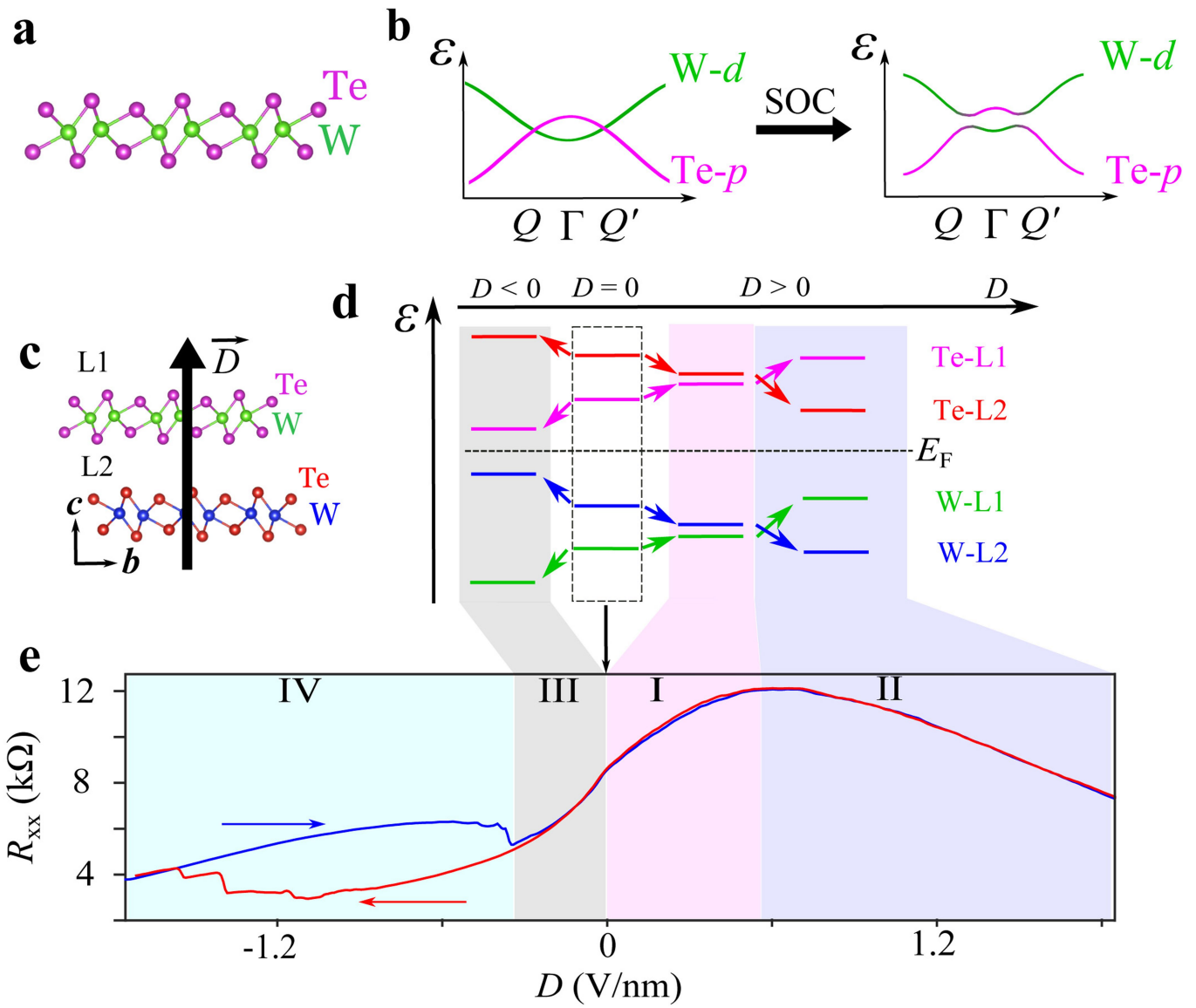

Extended Data Fig. 1 | Asymmetric inter-layer coupling. a, **b**, In monolayer WTe_2 (**a**), the low-energy physics is characterized by a W 5*d* band and a Te 5*p* band (**b**). Owing to the band inversion near the Γ point, a Dirac fermion is formed at the Q (Q′) point. Without spin–orbit coupling (SOC), the Dirac fermion is gapless because of the inversion symmetry of the 1T′ crystal structure[50]. The inclusion of spin–orbit coupling opens up a gap, leading to a quantum spin Hall state. **c**–**e**, Bilayer WTe_2 (**c**) is described by a pair of Dirac fermions at the Q point, which consist of four bands (**d**). To isolate the underlying mechanism for the resistance (R_{xx}) behaviour (**e**), we ignore the wavevector *k* and look at only the Γ point. The four bands simplify into four energy levels: the W 5*d* band in layer 1 (W-L1), the W 5*d* band in layer2 (W-L2), the Te 5*p* band in layer 1 (Te-L1) and the Te 5*p* band in layer 2 (Te-L2). Owing to the asymmetric inter-layer coupling, orbitals from opposite layers gain different on-site potentials, which lifts the layer degeneracy. This coupling is allowed only when the system lacks any symmetry that relates *c* to −*c* (Supplementary Information section II.4). An external *D* field along one direction enhances the layer splitting, whereas a *D* field along the opposite direction reduces and eventually reverses the splitting. The data in **e** can be explained by correlating the resistance with the global bandgap in **d**. The asymmetric-coupling mechanism is confirmed by our first-principles calculation (Extended Data Fig. 2). E_F, Fermi energy.

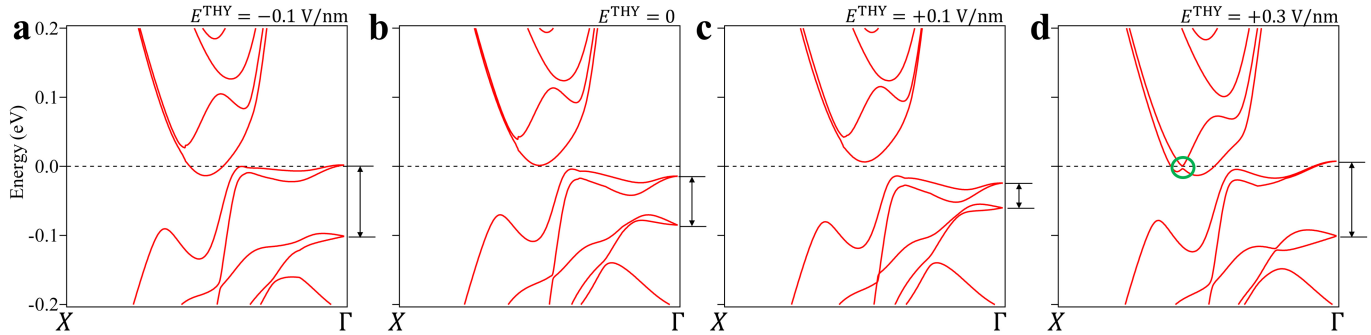

Extended Data Fig. 2 | Band structure of bilayer WTe_2 as a function of the external electric field. a–d, With positive E fields, the global bandgap increases then decreases; with negative E fields, the global bandgap decreases. The evolution of the valence-band splitting at the Γ point (black arrows) of the global bandgap as a function of the E field are consistent with the picture in Extended Data Fig. 1. The green circle in **d** highlights the anti-crossing (a massive Dirac fermion) formed between the lowest two conduction bands at $D > 0$. Such a massive Dirac cone with a small gap (approximately 3 meV) leads to large Berry curvature near the gap edges, which is responsible for the additional sharp features in the $V_{baa}^{2\omega}$ data (Supplementary Information section V).

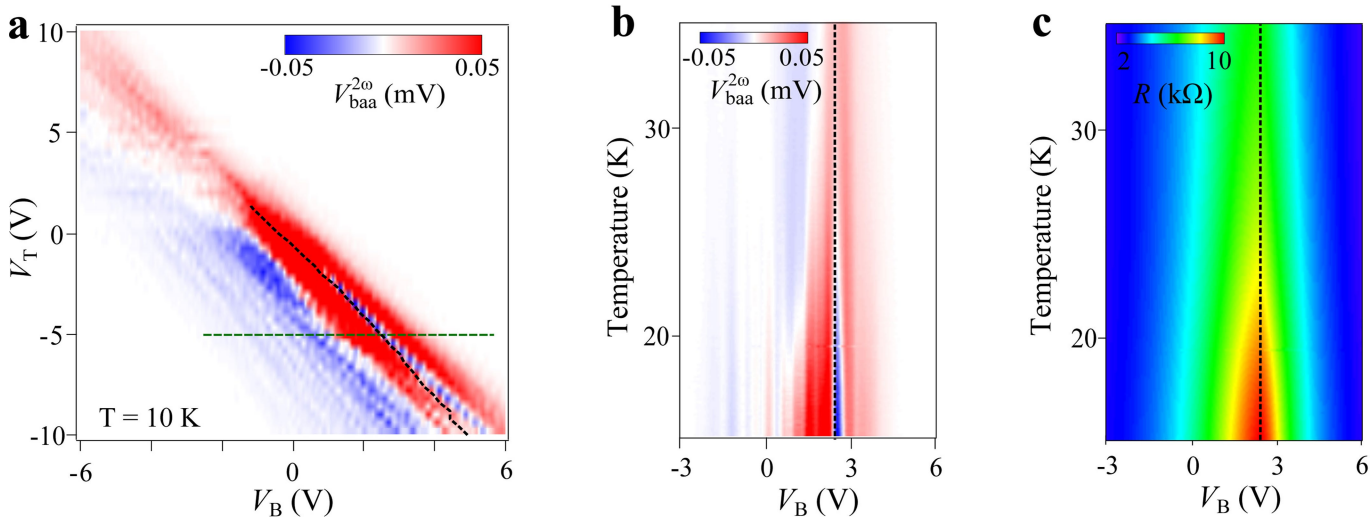

Extended Data Fig. 3 | Gate and temperature dependence of the nonlinear Hall voltage and resistance. a, Gate map of $V^{2\omega}_{baa}$. **b**, Temperature dependence of $V^{2\omega}_{baa}$ as a function of V_B at $V_T = -5$ V (green dashed line in **a**). **c**, Same as **b**, but for the resistance R. The diagonal black dashed line in **a** traces the maximum of the resistance as a function of V_T and V_B; the black dashed lines in **b** and **c** trace the resistance maximum at different temperatures.